Multiple lattice sites occupied AlTaO$_4$:Cr^{3+} phosphor for luminescence ratiometric thermometry and NIR light source

Lipeng Jiang [a], Liangliang Zhang [b], Xue Jiang [a,*], Guocai Lv [c], Yanjing Su [a,*]

[a] *Beijing Advanced Innovation Center for Materials Genome Engineering, Corrosion and Protection Center, University of Science and Technology Beijing, Beijing 100083, China*
[b] *State Key Laboratory of Luminescence and Applications, Changchun Institute of Optics, Fine Mechanics and Physics, Chinese Academy of Sciences, 3888 Eastern South Lake Road, Changchun 130033, China*
[c] *Basic Experimental Center of Natural Science, University of Science and Technology Beijing, Beijing 100083, China*

ABSTRACT

Cr^{3+}-doped near infrared (NIR) phosphors have promising applications in NIR light sources and optical temperature detection. The development of materials with high relative sensitivity and efficient broadband NIR luminescence is the key. In this paper, we report a new multifunctional NIR phosphor AlTaO$_4$:Cr^{3+}, which contains both narrow-band emission associated with $^2E_g \rightarrow ^4A_{2\ g}$ transition and broadband emission induced by the $^4T_{2\ g} \rightarrow ^4A_{2\ g}$ transition owing to Cr^{3+} occupies both AlO$_6$ and TaO$_6$ lattice sites. The R-line ($^2E_g \rightarrow ^4A_{2\ g}$) emission and its anti-Stokes phonon sideband emission follow the Boltzmann distribution, and the thermometer constructed accordingly reaches a maximum S$_r$ of 1% K^{-1} at 110 K. Under 425 nm excitation, the broad emission band (FWHM = 200 nm) reaches maximum at 880 nm with an internal quantum efficiency of 62.8%. The NIR LEDs prepared with AlTaO$_4$:Cr^{3+} confirm the application value in NIR light sources.

1. Introduction

In recent years, Cr^{3+}-doped near infrared (NIR) luminescence materials have been widely studied [1–7]. Cr^{3+} possesses a 3d^3 electron configuration and its 3d-3d electron transition is very sensitive to the crystal field environment of the host lattice [8,9]. When Cr^{3+} is in a strong crystal field, it shows a narrow band emission associated with $^2E_{2\ g} \rightarrow ^4A_{2\ g}$ transition. On the contrary, it will show a broadband emission induced by the spin-allowed $^4T_{2\ g} \rightarrow ^4A_{2\ g}$ transition [10–13]. Cr^{3+}-doped NIR luminescent materials can be applied to different fields based on the luminescent properties.

High efficiency broadband NIR phosphors are currently the most researched topic, which are mainly used in lighting, night vision, non-destructive testing, etc [6,14–18]. Researchers have reported numerous NIR phosphors with excellent performance in recent years, such as garnet (Ca$_2$LuZr$_2$Al$_3$O$_{12}$:Cr^{3+} [12,19], Gd$_3$Mg$_{0.5}$Al$_{1.5}$Ga$_{2.5}$Ge$_{0.5}$O$_{12}$:Cr^{3+} [20], Gd$_3$Sc$_{1.47}$Al$_{0.5}$Ga$_3$O$_{12}$:Cr^{3+} [21], et al.), phosphate (Sr$_9$Ga(PO$_4$)$_7$:Cr^{3+} [22], LiGaP$_2$O$_7$:Cr^{3+} [23], KAlP$_2$O$_7$:Cr^{3+} [24], et al.), silicate (Mg$_2$SiO$_4$:Cr^{3+} [25], LiInSi$_2$O$_6$:Cr^{3+} [26], et al.), tantalate (Mg$_4$Ta$_2$O$_9$:Cr^{3+} [27], MgTa$_2$O$_6$:Cr^{3+} [28], GaTaO$_4$:Cr^{3+} [29], et al.). However, the reported efficient NIR phosphors are concentrated in

shorter wavelengths (<850 nm), and broadband efficient NIR phosphors with long wavelength emission are still scarce.

Optical temperature detection is another focused area for Cr^{3+}-based NIR phosphors [30–32]. Among them, Boltzmann thermometry based on the luminescence intensity ratio (LIR) technique has proven to be particularly flexible and is considered as a simple and reliable technique for temperature measurement. It has the advantages of fast response time, noninvasive manner and high relative sensitivity (S$_r$) compared to conventional thermometers [33,34]. Researchers have demonstrated a variety of Cr^{3+}-doped NIR phosphors for optical temperature measurement, for example, Wang et al. constructed an optical thermometer with a maximum S$_r$ of 1.12% K^{-1} using La$_2$MgHfO$_6$:Cr^{3+} [35]. Back et al. studied the effect of the crystal field on the thermometric performance and constructed a Boltzmann thermometer with a maximum S$_r$ of 1.05% K^{-1} using α-Ga$_2$O$_3$ [36]. Although many Cr^{3+}-based materials for temperature measurement have been reported, most of the previous reports are mainly applicable at room temperature or higher. Thermometers with high S$_r$ and suitable for low temperature thermometry are still desirable.

In a previous study, Wei et al. reported AlTaO$_4$:Cr^{3+} for luminescence ratiometric thermometry with high S$_r$ (8.45% K^{-1}), where Cr^{3+}

---

* Corresponding author.
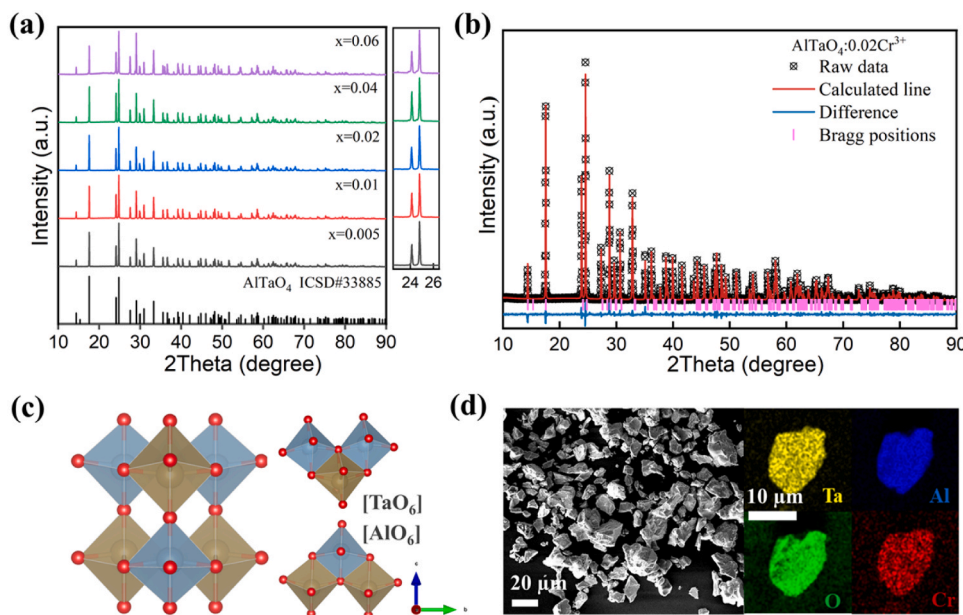*E-mail addresses:* jiangxue@ustb.edu.cn, yjsu@ustb.edu.cn (Y. Su).

Fig. 1. (a) XRD patterns of AlTaO$_4$: xCr^{3+}. (b) Rietveld refinement of AlTaO$_4$: 0.02Cr^{3+}. (c) The crystal structure of AlTaO$_4$. (d) SEM image and element distribution maps on the particle surface.

occupied AlO$_6$ site [37]. In this paper, multiple lattice sites occupied AlTaO$_4$:Cr^{3+} phosphor is reported, Cr^{3+} is demonstrated to occupy both AlO$_6$ and TaO$_6$ lattice sites. The Cr^{3+} occupying the AlO$_6$ octahedron possesses a strong crystal field, and the spin-forbidden $^2E_g{\rightarrow}^4A_{2\,g}$ transition is sensitive to temperature, and a highly sensitive (1% K^{-1} @110 K) LIR thermometer is constructed based on this feature. The Cr^{3+} occupying the TaO$_6$ octahedron has a weak crystal field with a broadband emission (FWHM = 200 nm) with a peak wavelength of 880 nm and an internal quantum efficiency (IQE) of 62.8% under 425 nm excitation. The NIR LED prepared with AlTaO$_4$: Cr^{3+} exhibits an output power of 30.4 mW at a drive current of 100 mA. These results demonstrate that AlTaO$_4$: Cr^{3+} is a promising multifunctional NIR phosphor.

2. Materials preparation and characterization

AlTaO$_4$: xCr^{3+} were prepared by solid-state reaction method. Ta$_2$O$_5$ (99.99%), Al$_2$O$_3$ (AR), Cr$_2$O$_3$ (AR) were adopted as starting materials. The raw materials, which were weighed and mixed well according to the stoichiometric ratio, sintered at 1520 °C for 7 h, cooled and ground to obtain the desired phosphors.

The XRD patterns were recorded by a BRUKER D8 ADVANCE X-ray diffractometer. GSAS software was utilized to Rietveld refinement. The Edinburgh FLS-1000 fluorescence spectrophotometer equipped with a 500 W Xe lamp as the excitation source was utilized to obtain excitation and emission spectra and fluorescence lifetimes. The temperature-dependent spectra were recorded by a FLS-1000 equipped with a variable-temperature liquid nitrogen optical cryostat Oxford Optistat DN2. The sample morphology was observed by scanning electron microscopy (TESCAN) and the elemental distribution was analyzed with the Oxford xplore 30 accessory equipped. The IQE was measured by an absolute PL quantum yield measurement system (Hamamatsu C9920–02). The output power of the NIR LED was recorded by using a HAAS 2000 photoelectric measuring system (350–1100 nm, EVERFINE, China).

3. Results and discussion

3.1. Crystal structure

The XRD patterns with different Cr^{3+} doping concentrations are

Table 1
Refinement data of AlTaO$_4$:xCr^{3+}.

x value	x = 0.02
Crystal system	Monoclinic
Space group	C 2/m
Lattice parameters	
a (Å)	12.1446
b (Å)	3.7747
c (Å)	6.4569
α/γ (°)	90
β(°)	107.74
Cell volume (Å^3)	281.975
R$_p$	6.12%
R$_{wp}$	8%
χ^2	2.018

provided in Fig. 1a. The XRD lines match well with the standard card (ICSD#33885) without any impurity phases. In the AlTaO$_4$ crystal, TaO$_6$ octahedra and AlO$_6$ octahedra are available for occupation by Cr^{3+} (0.615 Å) (Fig. 1c), where the radii of the six-coordinated Al^{3+} and Ta^{5+} are 0.535 Å and 0.64 Å, respectively. According to the ionic radii, the lattice expands when Cr^{3+} occupies Al^{3+} site and shrinks when it occupies Ta^{5+} site. However, the positions of the diffraction peaks do not shift as the doping concentration increases (right inset of Fig. 1a), suggesting that Cr^{3+} may not occupy a single site.

Fig. 1b shows the refinement pattern of AlTaO$_4$:0.02Cr^{3+}, and the refinement parameters are listed in Table 1 and Table S1. The refinement results show that AlTaO$_4$ belongs to monoclinic crystal system with C 2/m space group. There are four unequal O sites in AlTaO$_4$, and the AlO$_6$ and TaO$_6$ coordination octahedra are connected in a three-dimensional network by sharing O-O edges or O sites. SEM photographs show that the morphology of the prepared phosphor is irregularly shaped and the particle size is 10–30 µm (Fig. 1d). Elemental mapping results show that the constituent elements are uniformly dispersed on the sample surface. The EDS spectrum is provided in the Fig. S1 and the EDS test result is generally agreement with the design values (Table S2).
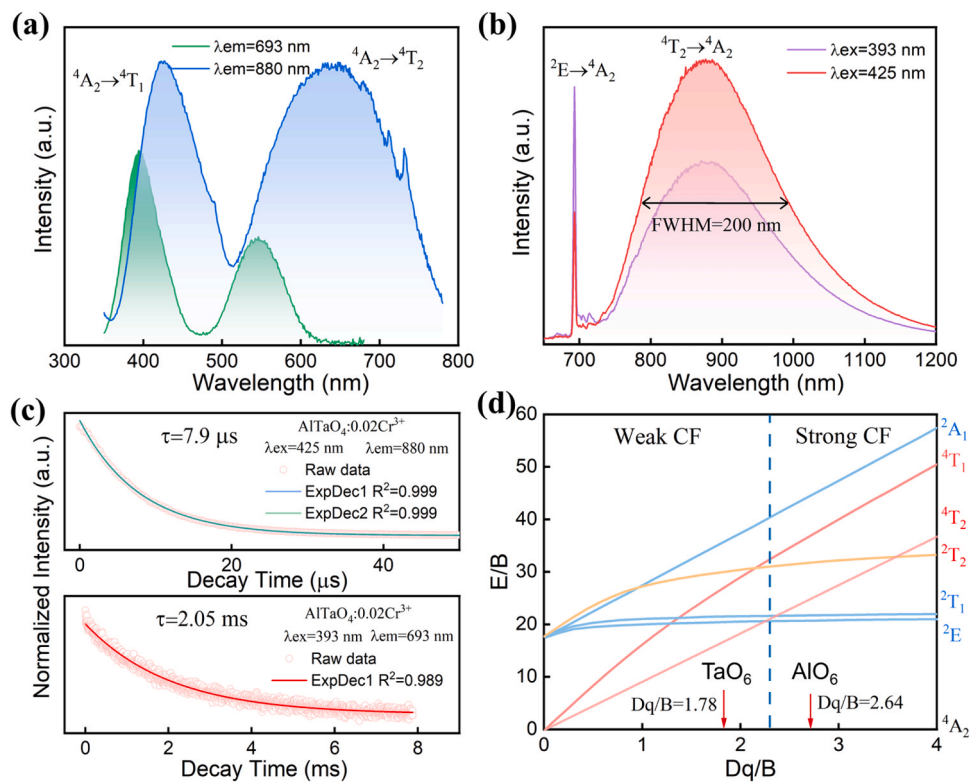
Fig. 2. (a) Excitation and (b) emission spectra of AlTaO$_4$:0.02Cr^{3+}. (c)Decay curves of AlTaO$_4$:0.02Cr^{3+} monitored at 880 nm and 693 nm. (d) Tanabe-Sugano energy level diagrams of Cr^{3+} ions in TaO$_6$ and AlO$_6$ sites.

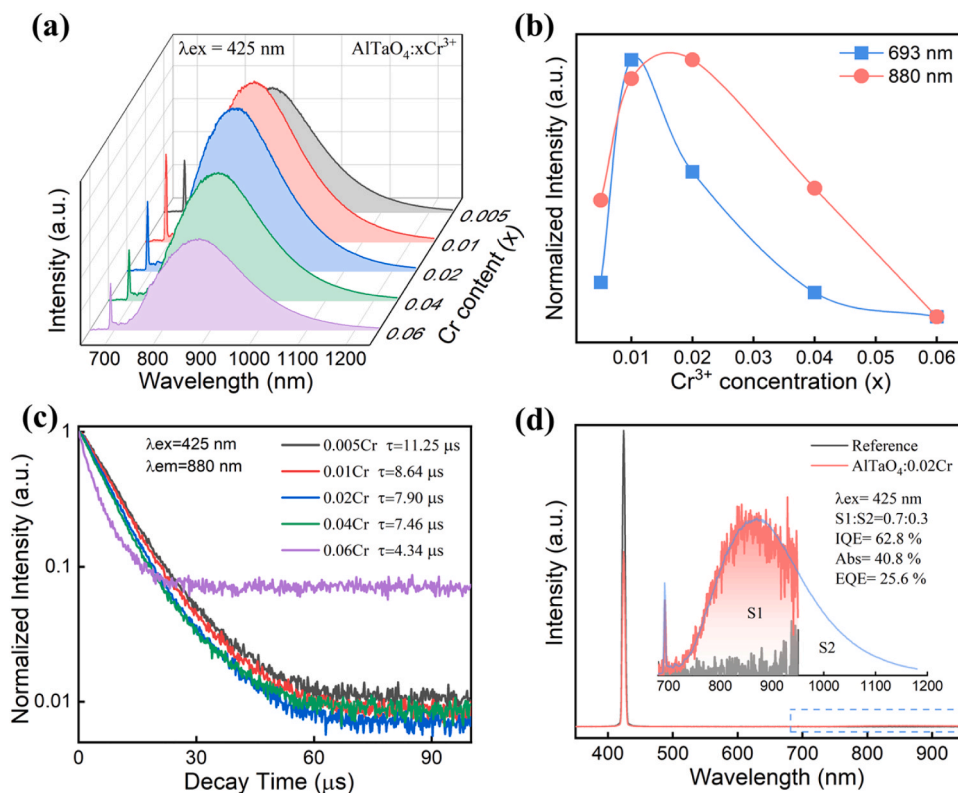**Fig. 3.** (a) Emission spectra of AlTaO$_4$:xCr^{3+} under excitation of 425 nm. (b) Normalized intensity of the emission bands located at 693 nm and 880 nm. (c) Decay curves. (d) IQE spectra of AlTaO$_4$:0.02Cr^{3+}.
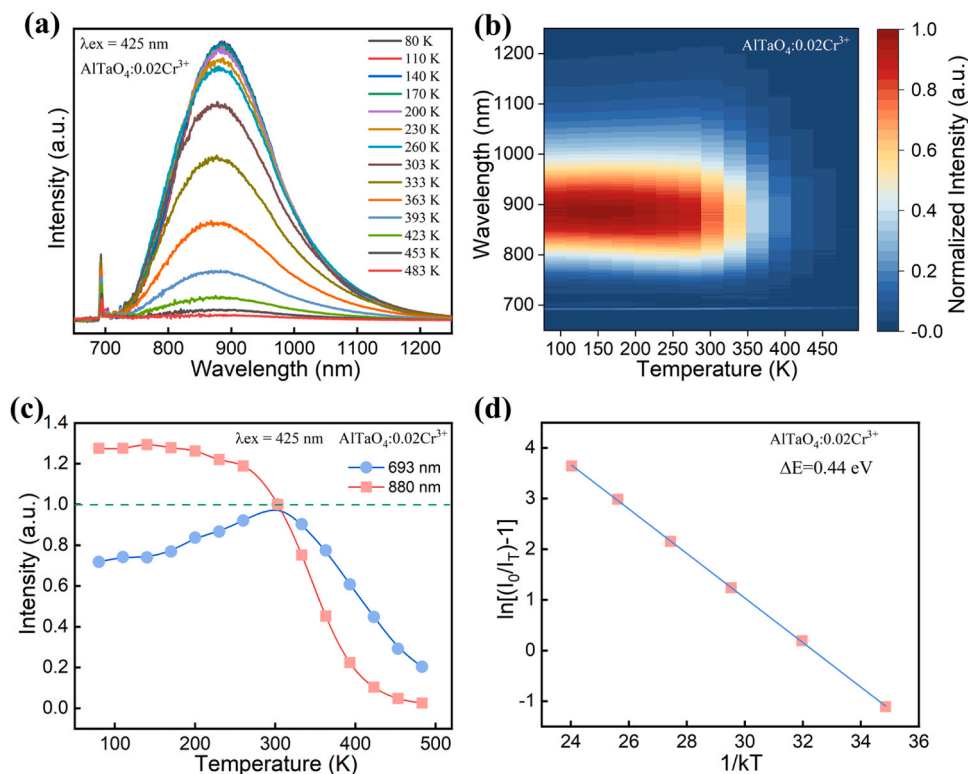
Fig. 4. (a) (b) Temperature-dependent emission spectra of $AlTaO_4:0.02Cr^{3+}$ under 425 nm excitation. (c) The normalized emission intensity versus temperature. (d) Linear fitting of $ln(I_0/I_T -1)$ with $1/kT$.

3.2. Photoluminescence properties induced by multi-lattice sites occupation

Fig. 2a and Fig. 2b present the excitation and emission spectra of $AlTaO_4:Cr^{3+}$. The emission spectrum of $AlTaO_4:Cr^{3+}$ consists of a broad band (880 nm, FWHM= 200 nm) and a narrow band (693 nm), and the large difference in energy between the two bands is unlikely to be due to the same luminescence center. There are two excitation bands in the excitation spectra, corresponding to the $^4A_{2g} \rightarrow ^4T_{1g}$ and $^4A_{2g} \rightarrow ^4T_{2g}$ transitions of Cr^{3+}. The absorption bands of the diffuse reflection spectrum correspond to the excitation spectrum (Fig. S2). The excitation spectra of $AlTaO_4:Cr^{3+}$ were measured by using 880 nm and 693 nm as monitoring wavelengths, and the peak positions of the excitation spectra show large differences, with the best excitation wavelengths of 425 nm and 393 nm, respectively. Under the excitation of 393 nm, the emission intensity at 693 nm shows a significant increase. Consequently, we believe that the two separated emission bands are caused by the simultaneous occupation of Al and Ta lattice sites by Cr^{3+}. The affiliation of these two bands can be distinguished by calculating the respective crystal field strengths, which can be calculated using Eq. (1) [38].

$$D_q = \frac{1}{6} Z e^2 \frac{r^4}{R^5} \qquad (1)$$

where Dq is the crystal field strength, Z is the anionic charge, e is the cationic charge; r is the radius of the d-wave function, R is the Cr-O bond length. Since the Al-O band length is smaller than Ta-O (Table S3), Cr^{3+} has a stronger crystal field when it occupies the AlO_6 octahedron. Therefore, the narrow-band emission at 693 nm originates from the $^2E_g \rightarrow ^4A_{2g}$ (R line) transition of Cr^{3+} in the AlO_6 octahedron, and the broadband emission located at 880 nm is induced by the $^4T_{2g} \rightarrow ^4A_{2g}$ transition of Cr^{3+} in the TaO_6 octahedron.

To further verify this, the decay curves at both 880 nm and 693 nm could be well fitted by the single exponential function (Fig. 2c) with fluorescence lifetimes of 7.9 μs and 2.05 ms, respectively. All these

results confirm that Cr^{3+} occupies two sites. The crystal field environment of Cr^{3+} at these two sites can be estimated by the ratio of the octahedral crystal field parameter Dq to the Racah parameter B [39–41].

$$10 \cdot D_q = E_a(^4T_2)$$

$$\frac{D_q}{B} = \frac{15 \cdot (x - 8)}{x^2 - 10 \cdot x} D_q \cdot x = E_a(\ ^4T_1) - E_a(\ ^4T_2) \qquad (2)$$

where $E_a(\ ^4T_1)$ and $E_a(\ ^4T_2)$ are the energy level positions of $^4T_1$ and $^4T_2$ respectively. The Dq/B values of Cr^{3+} in occupying AlO_6 and TaO_6 sites are calculated to be 1.78 and 2.64, respectively (Fig. 2d). The detailed spectral parameters are listed Table S4.

The emission spectra of $AlTaO_4:xCr^{3+}$ under excitation of 425 nm are given in Fig. 3a, the excitation spectra with different Cr^{3+} concentrations monitored at 880 nm are provided in Fig. S3. To observe whether the ratio of broadband to narrowband varies with increasing Cr^{3+} concentration, the normalized emission spectra are given in Fig. S4. With increasing Cr^{3+} doping concentration, the luminescence intensities at 693 nm and 880 nm show a tendency of increasing and then decreasing. The emission intensities at 693 nm and 880 nm reaches its maximum at x = 0.01 and x = 0.02, respectively (Fig. 3b). The emission intensity decreases gradually when the doping concentration continues to increase due to the concentration quenching. Since the optimum doping concentration at this point is the total design doping concentration, the actual alternative concentrations for the AlO_6 and TaO_6 positions are not available at this time.

The luminescence lifetime monitored at 880 nm decreases gradually from 11.25 μs to 4.34 μs with increasing Cr^{3+} concentration due to concentration quenching (Fig. 3c) [42,43]. The IQE of the optimal sample $AlTaO_4:0.02Cr^{3+}$ is 62.5% and the absorption efficiency is 40.8% under 425 nm excitation (Fig. 3d). The comprehensive performance of $AlTaO_4:0.02Cr^{3+}$ is better than that of many previously reported phosphors with peak wavelengths longer than 850 nm, such as $NaInP_2O_7$: Cr^{3+} (λem = 870 nm, FWHM =150 nm, IQE = 28.2%) [44], $NaScGe_2O_6$:
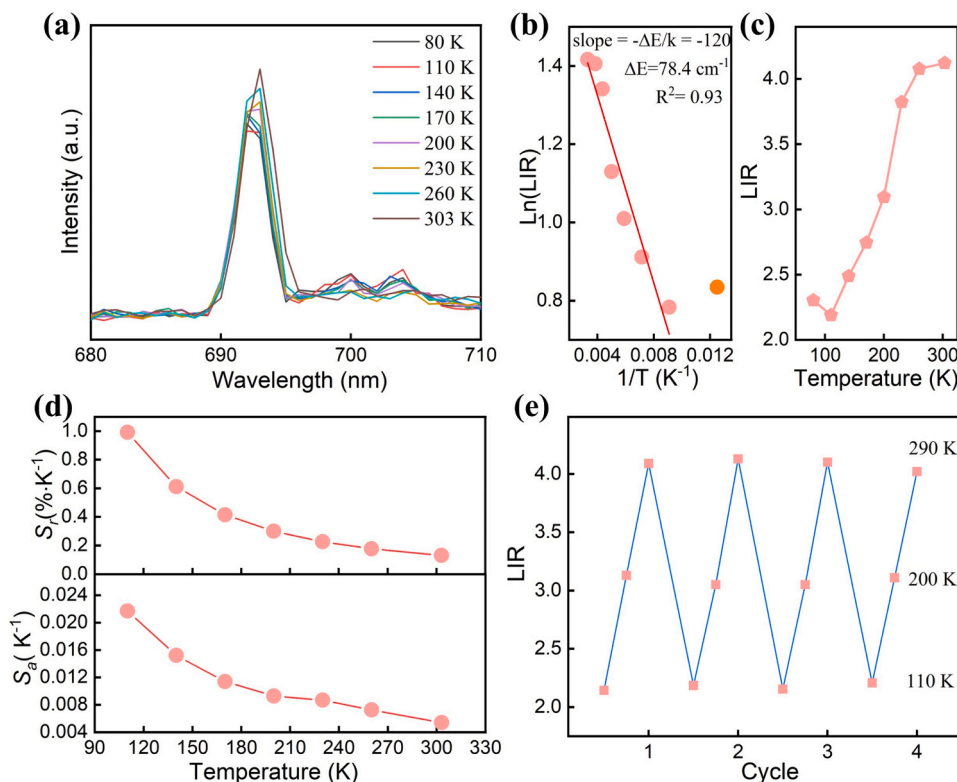
Fig. 5. Temperature-dependent (a) emission spectra, (b) Ln(LIR), (c) LIR, (d) S_r and S_a of AlTaO$_4$:0.02Cr^{3+}, (e) Heating–cooling cycle test of the LIR.

Cr^{3+} (λem = 895 nm, FWHM =162 nm, IQE = 40.22%) [41], Y0.57La$_{0.72}$Sc$_{2.71}$(BO$_3$)$_4$:Cr^{3+} (λem = 850 nm, FWHM = 172 nm, IQE = 41.1%) [45], Ga$_4$GeO$_8$:Cr^{3+} (λem = 850 nm, FWHM = 215 nm, IQE= 60%) [46], etc.

3.3. Thermal stability and spectroscopy application

Thermal stability is critical to the application of broadband NIR phosphors. The temperature-dependent emission spectra of AlTaO$_4$:0.02Cr^{3+} are given in Fig. 4a and b. The normalized intensities of the 693 nm and 880 nm emission bands in the temperature-dependent spectra under 425 nm excitation are shown in Fig. 4c. The broadband emission intensity decreases gradually with increasing temperature due to thermal quenching, and decreases sharply when the temperature is higher than 303 K. At 363 K, the emission intensity of AlTaO$_4$:0.02Cr^{3+} still keeps 45% of that at room temperature. The activation energy (ΔE) of AlTaO4:0.02Cr^{3+} is calculated according to the Arrhenius equation, as shown in Fig. 4d [47]. The ΔE of AlTaO$_4$:0.02Cr^{3+} in 303–483 K is 0.44 eV, which indicates its high energy barrier against thermal quenching. However, the thermal stability of AlTaO$_4$:0.02Cr^{3+} is not satisfactory, which may be attributed to the heterovalent substitution, resulting in more defects in the crystal [48].

In contrast to the broadband emission, the narrowband emission intensity at 693 nm (R line) increases first and then decreases with increasing temperature, showing a better thermal stability (77.4% @363 K). It is noted that the sideband emission peaks (700 nm and 704 nm), which are also asssociate with the $^2E_g \rightarrow ^4A_{2\,g}$ transition, show an opposite trend to the R-line in the 80–303 K (Fig. 5a). The local zoomed (697–706 nm) temperature-dependent emission spectra can be found in Fig. S5. Based on this feature, we investigat its feasibility for luminous ratio thermometry. The LIR is defined as the ratio of the integral intensities at 688–697 nm to the combined intensity of 700 nm and 704 nm (integral intensities at 697–706 nm). As can be seen from Fig. 5c, the LIR increases gradually with increasing temperature, except for 80 K. LIR is consistent with Boltzmann distribution:[31,37,49].

$$LIR = A\exp\left(-\frac{\Delta E}{kT}\right) \tag{3}$$

where A is a constant, ΔE is the energy gap of the thermally coupled state, k is the Boltzmann constant, T is the absolute temperature. Eq. (3) is equivalent to Eq. (4):

$$Ln(LIR) = Ln(A) - \frac{\Delta E}{kT} \tag{4}$$

The band gap can be obtained by linearly fitting Ln(LIR) and 1/kT. The fitting results show that the Ln(LIR) dot at 80 K deviates from the straight line and the band gap obtained by fitting the data from 110 to 303 K is 78.4 cm^{-1} (Fig. 5b). Then, S_r can be calculated by Eq. (5):

$$S_r = 100\% \times \left|\frac{dLIR}{dT}\frac{1}{LIR}\right| \tag{5}$$

Taking Eq. (3) into Eq. (5) gives Eq. (6):

$$S_r = \frac{\Delta E}{kT^2} \tag{6}$$

Fig. 5d depicts the S_r at different temperatures. The S_r decreases gradually with increasing temperature and possesses a maximum value of 1% K^{-1} at T = 110 K. This value is higher than some previously reported Cr^{3+}-based thermometers, such as Mg$_2$SiO$_4$:Cr^{3+}(0.7% K^{-1} @310 K) [50], Bi$_2$Ga$_4$O$_9$:Cr^{3+} (0.7% K^{-1} @90 K) [30], Sr$_{0.92}$Mg$_{0.91}$Al$_{10.1}$O$_{17}$:Cr^{3+}(0.43% K^{-1} @230 K) [51], β-Ga$_2$O$_3$: Cr^{3+}(0.64% K^{-1} @ 300 K) [36], and it is at the same level with La$_2$MgHfO$_6$:Cr^{3+} (1.12% K^{-1} @ 84 K) [35] and α-Ga$_2$O$_3$: Cr^{3+}(1.05% K^{-1} @300 K) [36]. However, in the low temperature range, the AlTaO$_4$: Cr^{3+} thermometer shows more advantageous in the thermal sensitivity.

The absolute sensitivities (S_a) is another important parameter, which can be defined as Eq. (7):
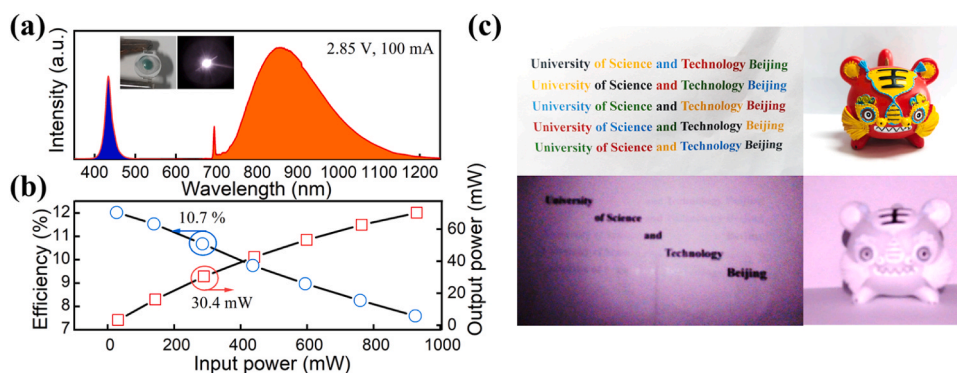
$$S_a = \left|\frac{dLIR}{dT}\right| \tag{7}$$

Fig. 6. (a) Luminescent spectrum of the NIR LED fabricated with AlTaO$_4$:0.02Cr^{3+}. (b) The output power and photoelectric efficiency at different input power. (c) Application of fabricated NIR LED for night vision.

The S$_a$ decreases gradually with increasing temperature with a maximum value of 0.0217 K^{-1} at 110 K (Fig. 5d) [33,36].

Additionally, we evaluated the temperature resolution δT and repeatability (R) of the thermometer through Eq. (8) and Eq. (9):

$$\delta T = \frac{\delta LIR/LIR}{Sr} \tag{8}$$

$$R\Big/\% = \left[1 - \frac{\max|LIR_{mean} - LIR_{every}|}{LIR_{mean}}\right] \times 100 \tag{9}$$

where δLIR/LIR is the relative uncertainty of LIR, which can be determined as the statistical relative standard deviation. The thermal cycling measurements were performed for four cycles (Fig. 5e), the average LIR values at 110 K is 2.17. The δLIR/LIR is calculated as ≈ 0.025, and δT is 2.5 K at 110 K. The thermal cycling measuremen results show that AlTaO$_4$:0.02Cr^{3+} possess good reversibility (98.4% 110 K).

3.4. NIR-LED performance

The NIR LED devices were prepared by combining AlTaO$_4$:Cr^{3+} phosphor with 435 nm chips. The device can be observed to emit blue-violet light by the naked eye and NIR light is captured by the NIR camera after power on. Fig. 6a shows the electroluminescence spectra (2.85 V, 100 mA) of the NIR LED fabricated with AlTaO$_4$:Cr^{3+}. Increasing input power from 26.8 to 925 mW, the output power gradually increases from 3.2 to 70.2 mW. The conversion efficiency of the device decreases from 12% to 7.58% due to the decrease of the LED chip efficiency (Fig. 6b). The NIR output power of the NIR LED device is identified as ∼30.4 mW at a drive power of 285 mW and the photoelectric conversion efficiency is calculated as 10.7%.

Based on the unique properties of NIR light, we demonstrate interesting applications with the prepared NIR LED (Fig. 6c). Under natural light, a conventional digital camera can clearly capture the colorful words of University of Science and Technology Beijing. Under NIR device illumination, the NIR camera can only clearly capture the black words on the diagonal. It is due to the presence of a large amount of black carbon in the black text, which has a stronger absorption of NIR light, while other colored texts show a weaker absorption of NIR light. The NIR camera can capture the toy tiger under the illumination of the NIR light source, which indicates that it can be used in night vision.

4. Conclusion

In conclusion, we prepared AlTaO$_4$:Cr^{3+} phosphor by high-temperature solid-state reaction method. The structural and spectroscopic analysis confirm that Cr^{3+} occupies both AlO$_6$ and TaO$_6$ lattice sites. A highly sensitive (1% K^{-1} @110 K) LIR thermometer was constructed based on the Boltzmann distribution between R-line

(^{2}E$_g$→^{4}A$_{2\,g}$) emission and its anti-Stokes phonon sidebands emissions. Under 425 nm excitation, the broadband emission (FWHM=200 nm) induced by the ^{4}T$_{2\,g}$→^{4}A$_{2\,g}$ transition reaches maximum at 880 nm with an IQE of 62.8%. The constructed NIR LED device exhibits competitive light output (30.4 mW) and conversion efficiency (10.7%) in the 700–1100 nm range at 100 mA. All results show that the phosphor shows great promise for NIR LED and optical temperature measurement applications.

CRediT authorship contribution statement

Lipeng Jiang: Conceptualization, Data curation, Formal analysis, Investigation, Writing – original draft. **Liangliang Zhang**: Formal analysis, Investigation, Writing – review & editing. **Xue Jiang:** Supervision, Writing – review & editing. **Guocai Lv:** Writing – review & editing. **Yanjing Su:** Supervision, Writing – review & editing.

Declaration of Competing Interest

The authors declare that they have no known competing financial interests or personal relationships that could have appeared to influence the work reported in this paper.

Data Availability

No data was used for the research described in the article.

Appendix A. Supporting information

Supplementary data associated with this article can be found in the online version at doi:10.1016/j.jallcom.2023.172544.

References

[1] F. Zhao, Z. Song, Q. Liu, Advances in chromium-activated phosphors for near-infrared light sources, Laser Photonics Rev. (2022), 2200380.

[2] P. Dang, Y. Wei, D. Liu, G. Li, J. Lin, Recent advances in chromium-doped near-infrared luminescent materials: fundamentals, optimization strategies, and applications, Adv. Opt. Mater. 11 (2023) 2201739.

[3] J. Zhong, Y. Zhuo, F. Du, H. Zhang, W. Zhao, J. Brgoch, Efficient and tunable luminescence in Ga$_{2-x}$In$_x$O3:Cr^{3+} for near-infrared imaging, ACS Appl. Mater. Interfaces 13 (2021) 31835–31842.

[4] J. Xiang, X. Zhou, X. Zhao, Z. Wu, C. Chen, X. Zhou, C. Guo, Ab initio site-selective occupancy and luminescence enhancement in broadband NIR emitting phosphor $Mg_7Ga_2GeO_{12}$:Cr^{3+}, Laser Photonics Rev. (2023), 2200965.

[5] L. Li, F. Pan, P.A. Tanner, K.-L. Wong, Tunable dual visible and near-infrared persistent luminescence in doped zinc gallogermanate nanoparticles for simultaneous photosensitization and bioimaging, ACS Appl. Nano Mater. 3 (2020) 1961–1971.

[6] Y. Zhu, A. Huang, T. Panczuk, C.H.-H. Hor, K.-L. Wong, L. Li, Persistent luminescence induced by the introduction of multi-valent Mn ions in K_2LiBF_6 (B = Al, Ga and In) fluoride phosphors, Chem. Eng. J. 430 (2022), 132421.

[7] L. Zhang, J. Zhang, Z. Hao, H. Wu, G. Pan, H. Wu, X. Zhang, Recent progress on Cr^{3+} doped broad band NIR phosphors, Chin. J. Lumin. 40 (2019) 1449.

[8] L. Zhang, D. Wang, F. Liu, H. Wu, G. Pan, H. Wu, Z. Hao, H. Zhang, J. Zhang, Minimizing bond angle distortion to improve thermal stability of Cr^{3+} doped near-infrared phosphor, Laser Photonics Rev. 17 (2023) 2300092.

[9] J. Zhang, L. Zhang, F. Liu, H. Wu, H. Wu, G. Pan, Y. Luo, Z. Hao, J. Zhang, Smaller stokes shift induced highly efficient broadband near infrared garnet phosphor, Laser Photonics Rev. 17 (2023) 2200586.

[10] L. Jiang, X. Jiang, J. Xie, T. Zheng, G. Lv, Y. Su, Structural induced tunable NIR luminescence of $(Y,Lu)_3(Mg,Al)_2(Al,Si)_3O_{12}$:$Cr^{3+}$ phosphors, J. Lumin. 247 (2022), 118911.

[11] H. Xiao, J. Zhang, L. Zhang, H. Wu, H. Wu, G. Pan, F. Liu, J. Zhang, Cr^{3+} activated garnet phosphor with efficient blue to far-red conversion for pc-LED, Adv. Opt. Mater. 9 (2021) 2101134.

[12] L. Zhang, S. Zhang, Z. Hao, X. Zhang, G-h Pan, Y. Luo, H. Wu, J. Zhang, A high efficiency broad-band near-infrared $Ca_2LuZr_2Al_3O_{12}$:Cr^{3+} garnet phosphor for blue LED chips, J. Mater. Chem. C 6 (2018) 4967–4976.

[13] L. Zhang, D. Wang, Z. Hao, X. Zhang, G.-h Pan, H. Wu, J. Zhang, Cr^{3+}-doped broadband NIR garnet phosphor with enhanced luminescence and its application in NIR spectroscopy, Adv. Opt. Mater. 7 (2019) 1900185.

[14] L. Jiang, X. Jiang, L. Zhang, Q. Liu, X. Mi, Z. Yu, G. Lv, Y. Su, Broadband near-infrared luminescence in garnet $Y_3Ga_3MgSiO_{12}$: Cr^{3+} phosphors, Inorg. Chem. 62 (2023) 4220–4226.

[15] L. Jiang, X. Jiang, J. Xie, H. Sun, L. Zhang, X. Liu, Z. Bai, G. Lv, Y. Su, Ultra-broadband near-infrared $Gd_3MgScGa_2SiO_{12}$: Cr, Yb phosphors: Photoluminescence properties and LED, Appl., J. Alloy. Compd. 920 (2022), 165912.

[16] F.Y. Zhao, H. Cai, S.Y. Zhang, Z. Song, Q.L. Liu, Octahedron-dependent near-infrared luminescence in Cr3+-activated phosphors, Mater. Today Chem. 23 (2022), 100704.

[17] Q. Yuan, D. Liu, P. Dang, H. Lian, G. Li, J. Lin, Two selective sites control of Cr^{3+}-Doped ABO_4 phosphors for tuning ultra-broadband near-infrared photoluminescence and multi-applications, Laser Photonics Rev. 16 (2022) 2100459.

[18] Y. Wang, Z. Wang, G. Wei, Y. Yang, S. He, J. Li, Y. Shi, R. Li, J. Zhang, P. Li, Ultra-broadband and high efficiency near-infrared $Gd_3Zn_xGa_{5-2x}Ge_xO_{12}$:$Cr^{3+}$ (x = 0–2.0) garnet phosphors via crystal field engineering, Chem. Eng. J. 437 (2022), 135346.

[19] S. He, L. Zhang, H. Wu, H. Wu, G. Pan, Z. Hao, X. Zhang, L. Zhang, H. Zhang, J. Zhang, Efficient super broadband NIR $Ca_2LuZr_2Al_3O_{12}$:Cr^{3+},Yb^{3+} garnet phosphor for pc-LED light source toward NIR spectroscopy applications, Adv. Opt. Mater. 8 (2020) 1901684.

[20] L. Jiang, X. Jiang, C. Wang, P. Liu, Y. Zhang, G. Lv, T. Lookman, Y. Su, Rapid discovery of efficient long-wavelength emission garnet: Cr NIR phosphors via multi-objective optimization, ACS Appl. Mater. Interfaces 14 (2022) 52124–52133.

[21] E.T. Basore, W. Xiao, X. Liu, J. Wu, J. Qiu, Broadband near-infrared garnet phosphors with near-unity internal quantum efficiency, Adv. Opt. Mater. 8 (2020) 2000296.

[22] F. Zhao, H. Cai, Z. Song, Q. Liu, Structural confinement for Cr^{3+} activators toward efficient near-infrared phosphors with suppressed concentration quenching, Chem. Mater. 33 (2021) 3621–3630.

[23] C. Yuan, R. Li, Y. Liu, L. Zhang, J. Zhang, G. Leniec, P. Sun, Z. Liu, Z. Luo, R. Dong, J. Jiang, Efficient and broadband $LiGaP_2O_7$:Cr^{3+} phosphors for smart near-infrared light-emitting diodes, Laser Photonics Rev. 15 (2021) 2100227.

[24] H. Zhang, J. Zhong, F. Du, L. Chen, X. Zhang, Z. Mu, W. Zhao, Efficient and thermally stable broad-band near-infrared emission in a $KAlP_2O_7$:Cr^{3+} phosphor for nondestructive examination, ACS Appl. Mater. Interfaces (2022).

[25] S. Miao, Y. Liang, D. Chen, R. Shi, X. Shan, Y. Zhang, F. Xie, X.-J. Wang, Site-selective occupancy control of Cr ions toward ultrabroad-band infrared luminescence with a spectral width up to 419 nm, ACS Appl. Mater. Interfaces 14 (2022) 53101–53110.

[26] X. Xu, Q. Shao, L. Yao, Y. Dong, J. Jiang, Highly efficient and thermally stable Cr3 +-activated silicate phosphors for broadband near-infrared LED applications, Chem. Eng. J. 383 (2020) 123108.

[27] W. Tang, D. Wu, Y. Xiao, X. Dong, Y. Wang, W. Zhou, Y. Liu, L. Zhang, An efficient perovskite-like phosphor with peak emission wavelength at 850 nm for high-performance NIR LEDs, Adv. Opt. Mater. 11 (2023) 2202237.

[28] G. Liu, M.S. Molokeev, B. Lei, Z. Xia, Two-site Cr^{3+} occupation in the $MgTa_2O^6$:Cr^{3+} phosphor toward broad-band near-infrared emission for vessel visualization, J. Mater. Chem. C. 8 (2020) 9322–9328.

[29] J. Zhong, Y. Zhuo, F. Du, H. Zhang, W. Zhao, S. You, J. Brgoch, Efficient broadband near-infrared emission in the $GaTaO_4$:Cr^{3+} phosphor, Adv. Opt. Mater. 10 (2022), 2101800.

[30] M. Back, E. Trave, J. Ueda, S. Tanabe, Ratiometric optical thermometer based on dual near-infrared emission in Cr^{3+}-doped bismuth-based gallate host, Chem. Mater. 28 (2016) 8347–8356.

[31] R. Li, G. Wei, Z. Wang, Y. Wang, J. Li, S. He, L. Li, H. Suo, W. Ding, P. Li, Cr^{3+}-facilitated ultra-sensitive luminescence ratiometric thermometry at cryogenic temperature, Laser Photonics Rev. 17 (2023) 2200589.

[32] M. Back, J. Ueda, M.G. Brik, S. Tanabe, Pushing the limit of boltzmann distribution in C_r^{3+}-Doped $CaHfO_3$ for cryogenic thermometry, ACS Appl. Mater. Interfaces 12 (2020) 38325–38332.

[33] K. Elzbieciak-Piecka, M. Suta, L. Marciniak, Structurally induced tuning of the relative sensitivity of $LaScO_3$:Cr^{3+} luminescent thermometers by co-doping lanthanide ions, Chem. Eng. J. 421 (2021), 129757.

[34] F. Vetrone, R. Naccache, A. Zamarrón, A. Juarranz de la Fuente, F. Sanz-Rodríguez, L. Martinez Maestro, E. Martín Rodriguez, D. Jaque, J. García Solé, J. A. Capobianco, Temperature sensing using fluorescent nanothermometers, ACS Nano 4 (2010) 3254–3258.

[35] Y. Wang, H. Suo, L. Li, G. Wang, W. Deng, W. Ding, Z. Wang, P. Li, Z. Zhang, Cr^{3+}-doped double-perovskites for near-infrared luminescent ratiometric thermometry, Phys. B: Condens. Matter 625 (2022), 413496.

[36] M. Back, J. Ueda, H. Nambu, M. Fujita, A. Yamamoto, H. Yoshida, H. Tanaka, M. G. Brik, S. Tanabe, Boltzmann thermometry in Cr^{3+}-Doped Ga_2O_3 polymorphs: the structure matters!, Adv. Opt. Mater. 9 (2021) 2100033.

[37] G. Wei, Z. Wang, R. Li, Y. Wang, L. Li, J. Li, Y. Shi, S. He, Y. Yang, H. Suo, P. Li, Ultra-sensitive luminescence ratiometric thermometry from $^2E{\rightarrow}^4A_2$ transitions of $AlTaO_4$:Cr^{3+}, Opt. Lett. 47 (2022) 6041–6044.

[38] L. Jiang, X. Jiang, Y. Zhang, C. Wang, P. Liu, G. Lv, Y. Su, Multiobjective machine learning-assisted discovery of a novel cyan–green garnet: Ce phosphors with excellent thermal stability, ACS Appl. Mater. Interfaces 14 (2022) 15426–15436.

[39] B. Struve, G. Huber, The effect of the crystal field strength on the optical spectra of Cr3+ in gallium garnet laser crystals, Appl. Phys. B 36 (1985) 195–201.

[40] H. Zeng, T. Zhou, L. Wang, R.-J. Xie, Two-site occupation for exploring ultra-broadband near-infrared phosphor—double-perovskite La_2MgZrO_6:Cr^{3+}, Chem. Mater. 31 (2019) 5245–5253.

[41] X. Zhou, W. Geng, J. Li, Y. Wang, J. Ding, Y. Wang, An ultraviolet–visible and near-infrared-responded broadband nir phosphor and its NIR spectroscopy application, Adv. Opt. Mater. 8 (2020) 1902003.

[42] C. Li, J. Zhong, Highly efficient broadband near-infrared luminescence with zero-thermal-quenching in garnet $Y_3In_2Ga_3O_{12}$:Cr^{3+} phosphors, Chem. Mater. 34 (2022) 8418–8426.

[43] L. Fang, L. Zhang, H. Wu, H. Wu, G. Pan, Z. Hao, F. Liu, J. Zhang, Efficient broadband near-infrared $CaMgGe_2O^6$:Cr^{3+} phosphor for pc-LED, Inorg. Chem. 61 (2022) 8815–8822.

[44] L. Zeng, J. Zhong, C. Li, Z. Zhuang, L. Chen, W. Zhao, Broadband near-infrared emission in the $NaInP_2O_7$:Cr^{3+} phosphor for light-emitting-diode applications, J. Lumin. 247 (2022), 118909.

[45] H. Wu, L. Jiang, K. Li, C. Li, H. Zhang, Design of broadband near-infrared $Y_{0.57}La_{0.72}Sc_{2.71}(BO_3)_4$:$Cr^{3+}$ phosphors based on one-site occupation and their application in NIR light-emitting diodes, J. Mater. Chem. C. 9 (2021) 11761–11771.

[46] L. Yao, Q. Shao, M. Shi, T. Shang, Y. Dong, C. Liang, J. He, J. Jiang, Efficient ultra-broadband Ga_4GeO_8:Cr^{3+} phosphors with tunable peak wavelengths from 835 to 980 nm for NIR pc-LED application, Adv. Opt. Mater. 10 (2022) 2102229.

[47] L. Jiang, X. Zhang, H. Tang, S. Zhu, Q. Li, W. Zhang, X. Mi, L. Lu, X. Liu, A Mg^{2+}-Ge^{4+} substituting strategy for optimizing color rendering index and luminescence of YAG: Ce^{3+} phosphors for white LEDs, Mater. Res. Bull. 98 (2018) 180–186.

[48] Y. Yang, Z. Lu, H. Fan, M. Chen, L. Shen, X. Zhang, Q. Pang, J. Chen, P. Chen, L. Zhou, Ultra-broadband near-infrared phosphors realized by the heterovalent substitution strategy, Inorg. Chem. 62 (2023) 3601–3608.

[49] S.A. Wade, S.F. Collins, G.W. Baxter, Fluorescence intensity ratio technique for optical fiber point temperature sensing, J. Appl. Phys. 94 (2003) 4743–4756.

[50] Z. Ristić, V. Đorđević, M. Medić, S. Kuzman, M. Sekulić, Ž. Antić, M.D. Dramićanin, Triple-temperature readout in luminescence thermometry with Cr3+-doped Mg_2SiO_4 operating from cryogenic to physiologically relevant temperatures, Meas. Sci. Technol. 32 (2021), 054004.

[51] L. Zheng, J. Kuang, J. Shen, H. Wu, H. Wu, Y. Luo, G.-H. Pan, Z. Hao, L. Zhang, J. Zhang, Spectral broadening in Cr^{3+}-Doped $Sr_{0.92}Mg_{0.91}Al_{10.1}O_{17}$ NIR phosphor realized by multi-crystallographic site occupation, ACS Appl. Opt. Mater. (2023).